Aerothermal Analysis of the Project Fire II Afterbody Flow

Michael Wright,* Mark Loomis,† and Periklis Papadopoulos‡
NASA Ames Research Center, Moffett Field, California 94035

Computational fluid dynamics is used to simulate the afterbody heating of the Project Fire II ballistic reentry to Earth at 11.35 km/s. Results are obtained over a portion of the trajectory between the initial heat pulse and peak afterbody heating. Although forebody convective heating results are in excellent agreement with previous computations, initial noncatalytic predictions of afterbody heating were a factor of two below the experimental values. However, analogy with currently manufactured thermal protection materials suggests that significant catalysis may be occurring on the afterbody heat shield. Computations including finite rate catalysis are in good agreement with the data over the early portion of the trajectory, but are conservative near the peak afterbody heating point, especially on the rear portion of the conical frustum. Further analysis of the flight data from Fire II shows that peak afterbody heating on the frustum occurs before peak forebody heating, a result that contradicts computations and flight data from other entry vehicles. This result suggests that another mechanism, possibly pyrolysis, may be occurring during the later portion of the trajectory, resulting in less total heat transfer than the current predictions.

Nomenclature

$\mathcal{D}_{N_2-N_2}$	=	reference binary diffusion coefficient, m^2/s
Kn_{GLL}	=	gradient length local Knudsen number
L	=	afterbody reference length, m
M_s	=	molecular weight of species s, kg/mol
$\dot{q}_{cat}$	=	catalytic component of heat transfer, W/cm^2
$\dot{q}_{tot}$	=	total convective heat transfer, W/cm^2
$\mathcal{R}$	=	universal gas constant, $J/(mol \cdot K)$
Re_c	=	cell Reynolds number
Re_D	=	freestream Reynolds number based on body diameter
s	=	pathlength distance from nose, m
T	=	translational–rotational temperature, K
T_w	=	wall temperature, K
t	=	time, s
$\dot{w}_s$	=	species production rate, $kg/(m^3 \cdot s)$
x	=	axial distance along afterbody, m
γ_s	=	species accommodation coefficient
ϵ	=	surface emissivity
ν_s	=	species diffusion velocity, m/s
ρ_s	=	species density, kg/m^3
σ	=	Stefan–Boltzmann constant, $W/(m^2 \cdot K^4)$
ϕ	=	circumferential location on afterbody

Introduction

THE Project Fire II ballistic reentry to Earth at a nominal velocity of 11.35 km/s 37 years ago remains one of the best sources of aerothermal heating data for the design of sample return capsules. The data from this flight experiment[1−3] encompass both the thermochemical nonequilibrium and equilibrium flow regimes and include measurements of both radiative and total heating on the forebody and afterbody. Because of the quality of these data, a number of researchers have performed computational fluid dynamics (CFD) simulations of the forebody of the Fire II entry vehicle,[4−8] with generally good results. In particular, Olynick et al.[4] coupled a Navier–Stokes solver with a nonequilibrium radiation code and showed good agreement for stagnation point heat transfer over the Fire II trajectory between 1634 and 1651 s (77–37 km altitude), a period that encompassed the peak forebody heating point, $t = 1644.5$ s. However, in most cases the primary motivation of the previous work was to model the coupling between shock-layer radiation and aerothermodynamics, and thus, the simulations concentrated on the forebody flow only. To our knowledge there have been no prior published attempts to reproduce the afterbody heating data presented in Ref. 3.

Uncertainties in afterbody heating predictions can have a significant impact on thermal protection system material selection and weight. Conservatism in the afterbody heat shield design will shift the center of gravity backward, reducing stability and in some cases necessitating ballast in the nose. Current design practices for afterbody heatshields typically assume a laminar, fully catalytic, nonablating surface. The predictions thus obtained are augmented by a large factor of safety to account for turbulent transition and uncertainty in the baseline computations. The main reason for this uncertainty is a sparsity of data for validation of our computational tools. Ground-test data are typically complicated by sting interference effects, although a limited amount of shock-tunnel data are available.[9] Little flight data at the appropriate entry velocities exist, and recent attempts to propose dedicated flight experiments have failed to reach fruition. Therefore, it is important to understand the limited flight data that are available to improve the design fidelity of the next generation of Earth and planetary entry vehicles and to assess the need for additional flight data. In this paper, we take a first step toward an understanding of the afterbody heating data from the Project Fire II flight experiment.

Reentry Vehicle Geometry and Instrumentation

The Fire II reentry vehicle consisted of a multilayer configuration made up of three phenolic–asbestos heat shields sandwiched between beryllium calorimeters. Figure 1, taken from Ref. 3, is a schematic of the vehicle showing the configuration of each calorimeter. The first two calorimeters and their associated heat shields were designed to be ejected after the onset of melting, yielding three separate data-gathering periods. Forebody instrumentation consisted of thermocouples and forward-looking radiometers. (See Refs. 1 and 2 for details on forebody instrumentation and placement.)

The 66-deg included angle conical afterbody section was constructed of a fiberglass shell supporting a layer of phenolic–asbestos

*Senior Research Scientist, Eloret Corporation. Senior Member AIAA.
†Research Scientist, Reacting Flow Environments Branch. Senior Member AIAA.
‡Senior Research Scientist, Eloret Corporation.

thermal protection material. A thin surface coating of silicon elastomer was added for prelaunch moisture protection. The conical frustum portion of the afterbody was instrumented with a symmetrical array of 12 gold calorimeters, distributed at three circumferential locations and four x stations on the frustum, as shown in Fig. 1. In addition, a single rearward-facing radiometer was placed on the frustum, also shown in Fig. 1. Details of the afterbody instrument placement are given in Table 1. The published accuracy of the thermocouples at the base of each calorimeter was ±28 K over the measured temperature range.[3] Raw temperature data were converted to estimates of total surface heat transfer by a curve-fitting procedure.[10] Uncertainty in the final heat transfer obtained is not given; however, we assume here that the uncertainty in the computation of the temperature gradient is of the same order as the uncertainty in T. This, coupled with published uncertainties in other steps of the data reduction process,[10] yield an estimated total uncertainty in heat transfer of ±15%. The rearward-facing radiometer indicated zero radiation during the entire entry with the exception of one brief pulse correlated to a forebody heatshield ejection event. Because the intensity threshold of the radiometer was approximately 1 W/cm^2 in the 0.2–4.0 μm range, and because the single flash indicated that the radiometer was indeed functioning, it is concluded that the afterbody heating rates consisted mainly of convective heating.[3] Further details on the instrumentation and data reduction procedures are available in Refs. 3 and 10.

Although the published reports give sufficient information to determine accurately the forebody geometry, complete information for the entire vehicle is more difficult to obtain. By compiling geometrical data from several sources,[1,3,11] we were able to construct an accurate (although somewhat simplified) outer mold line (OML) for the first heat shield configuration, shown in Fig. 2. The primary simplification that was made during construction of the OML was the elimination of the C-band antenna, which can be seen at the base of the vehicle in Fig. 1. This modification was made to allow for axisymmetric solutions to be obtained (three-dimensional antenna), and also because exact dimensions for the antenna could not be located. Because all instrumentation was placed on the conical frustum well away from the C-band antenna, this approximation should not greatly affect the computed results. In addition, a small backward-facing step resulting from the attachment of the

Table 1   Instrument placement on Fire II afterbody

Station[a]	Sensor type	x/L
2	Beginning of frustum	0
3	3 Calorimeters $\phi = 0, 120, 240$ deg[b]	0.19
4	1 Radiometer $\phi = 203.45$ deg	0.32
5	3 Calorimeters $\phi = 0, 120, 240$ deg	0.38
6	3 Calorimeters $\phi = 0, 120, 240$ deg	0.56
7	3 Calorimeters $\phi = 0, 120, 240$ deg 1 Pressure sensor, $\phi = 265$ deg	0.70
8	Theoretical cone apex	1.0

[a]Station numbers and x/L locations refer to Fig. 1.
[b]Circumferential location of the sensor.

Fig. 2   Relevant dimensions (in centimeters) of the Fire II reentry vehicle OML as modeled in the CFD simulations.
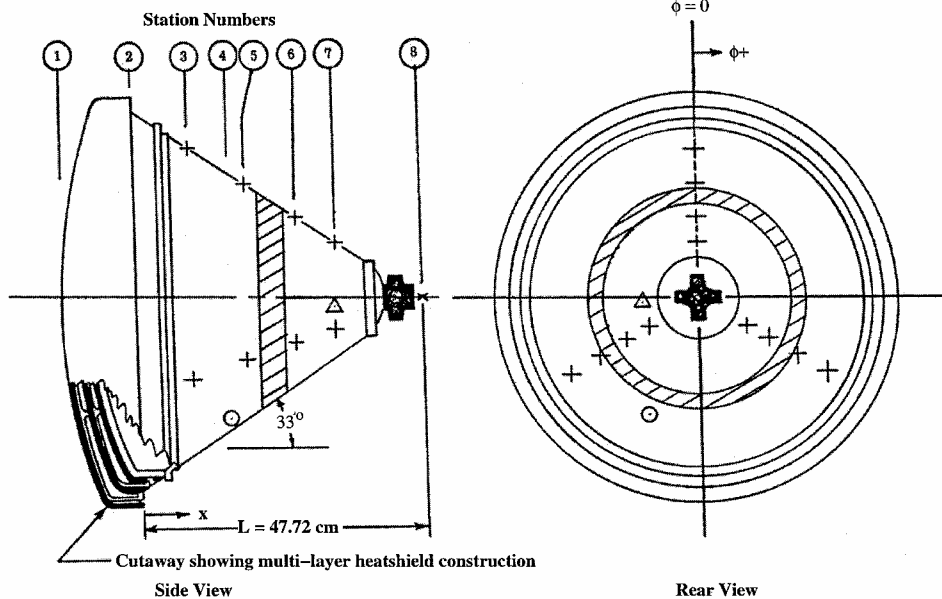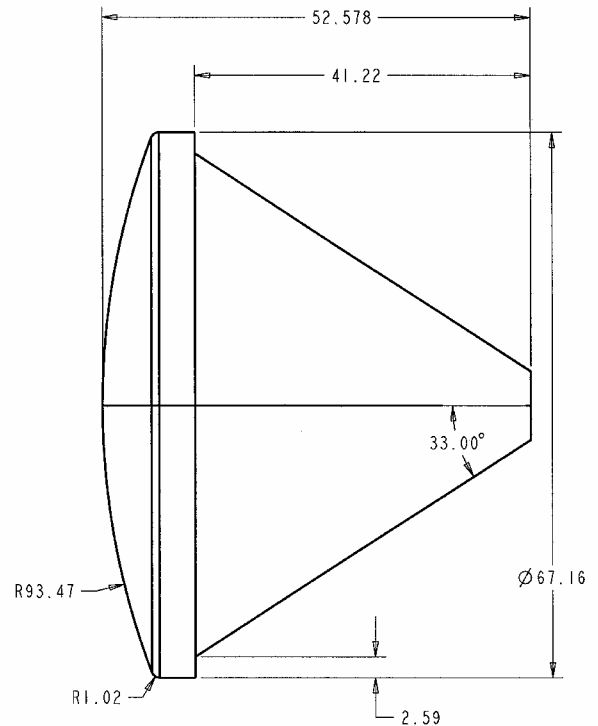

Fig. 1   Schematic of Fire II reentry vehicle showing multiple forebody heatshields and afterbody instrument placement; station numbers correspond to Table 1 (adapted from Ref. 3): +, gold calorimeter; △, pressure sensor; and ○, rediometer.

third forebody heatshield to the vehicle was eliminated, again due to a lack of geometric information.

As stated earlier, the forebody consisted of three calorimeter/heat shield combinations that were designed to be ejected after the onset of melting. This configuration effectively divided the data-gathering window into three discrete periods, interspersed with brief periods where the heatshield ejection process and resultant flowfield interaction made accurate data gathering impossible. The data periods bracket the peak forebody heating portion of the entry trajectory. Although the nominal angle of attack of the vehicle was 0 deg, the heatshield ejection process introduced significant off-axis forces to the reentry vehicle which resulted in successively larger angles of attack with time. Based on flight telemetry data, the angle of attack was less than 1 deg for the first data period, 5 deg during the second, and as much as 11 deg during the third period.[3] For this and other reasons (discussed later), the analysis presented here is limited to the first data period, which spans the onset of significant afterbody heating to the peak heating period on the conical frustum.

Physical and Numerical Modeling

A detailed description of the relevant equations for reentry flows has been presented in a number of sources[12–14] and will not be repeated here. Velocities during the portion of the Fire II trajectory considered here were in excess of 11 km/s at an altitude range between 75 and 60 km. At these conditions, the postshock flowfield is in a state of thermal and chemical nonequilibrium, and a significant amount of ionization is expected. Therefore, the flow is modeled using an 11-species (N_2, O_2, NO, N, O, N_2^+, O_2^+, NO^+, N^+, O^+, and e), 47-reaction finite rate air chemistry model. The chemical source terms are modeled using rates from Park,[15] with the exception of the rates for the electron impact ionization reactions, which are taken from Wilson.[16] The governing temperature for the electron impact ionization reactions is assumed to be the heavy particle translational temperature T based on earlier work by Olynick et al.[4] The translational temperature was used for consistency with the single-temperature interpretation of the data performed by Wilson.[16] The flow is modeled assuming thermal nonequilibrium, with separate equations for conservation of vibrational and total energies. The coupling between the translational and vibrational energy modes is modeled using a Landau–Teller formulation, where relaxation times are obtained from Millikan and White,[17] and assuming simple harmonic oscillators.

Viscous transport and thermal conductivity are modeled using the collision integral fits together with the mixing rule presented by Gupta et al.[18] The bifurcation method[19] is used to model binary diffusion, with the reference binary diffusion coefficient ($\mathcal{D}_{N_2-N_2}$) computed using the Gupta et al.[18] fits. This method allows for variations in species diffusion coefficients to be modeled without sacrificing the requirement that the diffusion velocities sum identically to zero. The diffusion velocity of the electrons is computed from the requirement of zero current density in the flow. The entire flowfield is assumed to be laminar, which should be a good assumption given the low freestream Reynolds numbers (Table 2) during the early portion of the entry. The assumption of laminar flow in the near wake was justified using blunt-body separation shear layer and inner wake transition correlations given by Lees.[20] Even for the final (highest Reynolds number Re) trajectory point simulated, the local Reynolds number in the shear layer was more than an order of magnitude below the transition Reynolds number, and the wake transition correlation indicated laminar flow for more than 11 body

diameters downstream. Because the sonic point in the neck region was only about 2.5 diameters downstream, we conclude that transition will not affect the separated flow region.

Surface catalysis is modeled using a diffusion limited approach,[21] in which the rate of production of a species at the wall is balanced by the rate of mass diffusion of the constituent species, that is,

$$\rho_s v_s|_w = \dot{w}_s|_w$$

where $v_s|_w$ is body-normal diffusion velocity of species s at the wall and $\dot{w}_s|_w$ is the rate of production, modeled with a first order reaction rate as

$$\dot{w}_s|_w = \rho_s \gamma_s \sqrt{\mathcal{R}T_w/2\pi M_s}$$

where γ_s is an accommodation coefficient representing the fraction of atoms or ions that recombine on reaching the wall.

We assume that the surface of the beryllium forebody is completely oxidized by the high concentration of O atoms in the shock layer and is, thus, noncatalytic to neutral species ($\gamma_{\text{neutrals}} = 0$). However, the surface is assumed to be charge neutral and, thus, fully catalytic to ion recombination ($\gamma_{\text{ions}} = 1$) (Ref. 21). This assumption was shown previously[4] to yield stagnation point heat transfer predictions in good agreement with the flight data. In addition, although the catalycity of oxidized beryllium in a reentry environment is not known, there is a large amount of experimental data indicating that oxidized metals are much less catalytic than their "clean" counterparts[22–23] and that an oxide with low electrical conductance, such as beryllium oxide, should be a poor catalyst. The afterbody surface coating is silicon elastomer, which was also initially assumed to be noncatalytic to neutral species and fully catalytic to ions. This assumption will be examined further in the "Results" section. An isothermal wall boundary condition was applied on the highly conductive metallic forebody, with the wall temperature at each time period taken from the thermocouple data. Both a cold wall condition and a radiative equilibrium wall boundary condition were considered for the afterbody, with details given in the "Results." A no-slip wall velocity boundary condition was applied on the entire surface. Freestream conditions were based on atmospheric soundings taken immediately after the flight.[11]

The CFD code used to obtain solutions for this paper was DPLR-Axi.[24] DPLR-Axi is a parallel multiblock axisymmetric extended Navier–Stokes solver, based on algorithms developed in GIANTS,[4] that incorporates all of the physical models discussed earlier. The Euler fluxes are computed using a modified form of Steger–Warming flux vector splitting (see Ref. 25) which significantly reduces the dissipation of the original scheme. Third-order spatial accuracy is obtained through MUSCL extrapolation, coupled with a minmod limiter.[26] Time advancement to a steady-state solution is achieved using the data-parallel line relaxation method.[24] This code has been successfully applied to several problems.[27,28] DPLR-Axi typically required about 10,000 iterations to reach a steady-state solution on the baseline (161 × 97) single-block grid (as compared to about 1000 iterations for a forebody only case) and required approximately 33 CPU h on a SGI R12000 workstation. The large-scale flow features were set up fairly quickly, but the afterbody heat transfer, especially on the flat base plate, converged to its final answer slowly.

Wake flows can be sensitive to details of the volume grid construction and care must be taken to generate a grid that is well aligned to the flow features. In particular, it is important to capture accurately the rapid expansion around the shoulder, which determines the thermochemical state of the essentially frozen wake. The nature of the separated flow region is also determined in large part by the shear layer and wake compression region.[29] At higher Reynolds numbers, the wake will consist of multiple counter-rotating vortices, which must be resolved.[30] Finally, care must be taken to ensure that the grid completely encloses the subsonic portion of the wake, which can extend several body diameters downstream. For this paper, solutions were obtained using two grid topologies. The first topology, shown in Fig. 3a, consists of a single mesh block constructed using a hyperbolic grid generator[31] to ensure orthogonality at the surface. The

Table 2   Fire II trajectory points and freestream conditions

Time,[a] s	Altitude, km	Re_D[b]	Velocity, km/s	Density, kg/m^3	T_∞, K	T_w, K
1634	76.42	2×10^4	11.36	$3.72e{-}5$	195	615
1636	71.04	5×10^4	11.31	$8.57e{-}5$	210	810
1637.5	67.05	7×10^4	11.25	$1.47e{-}4$	228	1030
1639	63.11	1×10^5	11.14	$2.41e{-}4$	242	1325
1640.5	59.26	2×10^5	10.97	$3.86e{-}4$	254	1560

[a]Seconds after launch.   [b]Freestream Reynolds number based on body diameter.
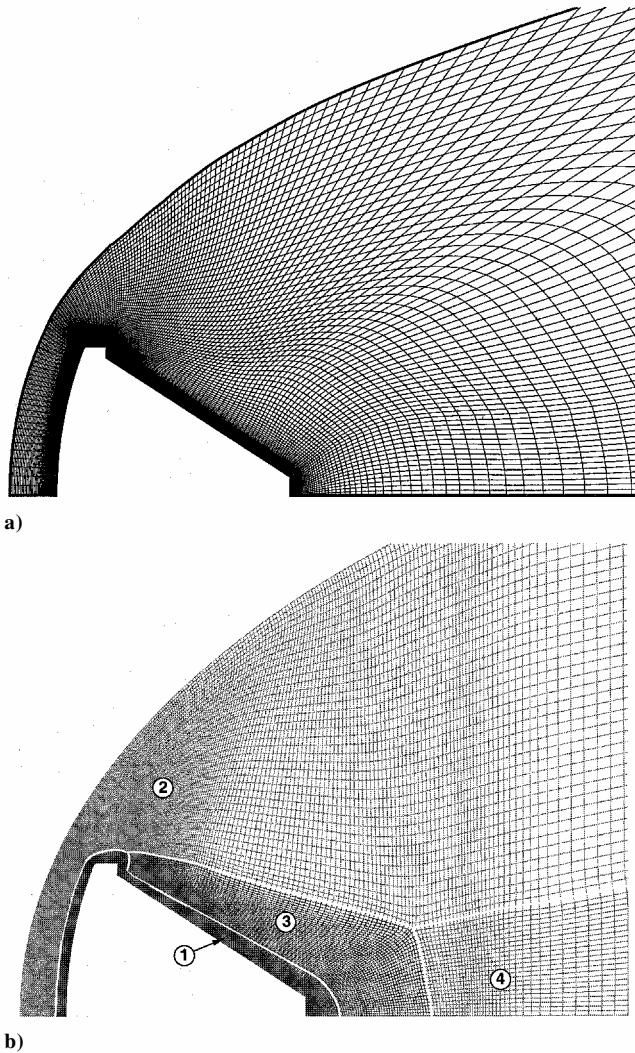
a)

b)

Fig. 3 Grid topologies used, with white lines to delineate elemental blocks, enlarged to show detail near the body surface: a) single-block hyperbolic grid and b) four-block grid with compact enrichment in wake region.

solution adaptive grid code SAGE[32] is used to fit the boundary to the computed shock. This topology allows for rapid grid generation and solution turnaround and should be adequate for preliminary heat shield design, as well as for the computation of low Reynolds number flows where the wake structure is dominated by a single large vortex. However, because the Reynolds number increases and the wake becomes more complex, it is desirable to use a grid topology that allows for compact enrichment of the separated flow region without propagation of the grid points throughout the rest of the grid. The second grid (Fig. 3b), constructed using GridPro,[33] allows for compact enrichment with a topology that results in 36 elemental blocks, mergeable into 4. With such a topology, the grid in the separation region can be arbitrarily densified without increasing the point density in the rest of the grid. With either topology, SAGE[32] is used to adapt the grid to the computed solution and cluster points near flow features of interest.

Results

Solutions were obtained for five trajectory points during the first data period, with freestream conditions listed in Table 2. The solutions range from 1634 to 1640.5 s after launch, which spans the period from the first appreciable afterbody heat transfer measurements to a point near peak afterbody heating. Solutions were limited to the first data period for several reasons, including the desire for laminar axisymmetric steady flow and the lack of complete geometric information for the second and third forebody calorimeter

configurations. Note that the final trajectory point, at $t = 1640.5$ s, occurs after the onset of forebody calorimeter melting. Therefore, it is possible that the accuracy of the afterbody data may be compromised by beryllium droplets entrained in the wake. However, the temperature vs time traces for the afterbody thermocouples show no anomalous readings that can be traced to forebody melting.

Wake Structure

Figure 4 shows streamlines in the separated flow region for all five trajectory points. All solutions were obtained on the baseline single-block grid, which has 161 points along the body surface and 97 points in the normal direction. At the lowest Reynolds number point ($t = 1634$ s) the flow separates on the conical frustum well after the heatshield shoulder, and is dominated by a single large vortex. As the Reynolds number (and t) increases, the separated flow region becomes larger and more complex, as would be expected for a laminar flow. At $t = 1636$ and 1637.5 s, the flow separates at the rearward-facing step after the shoulder, but remains dominated by a single vortex. However, by $t = 1639$ s a bulge can be seen about a third of the way down the conical frustum, which can be further resolved into a small secondary vortex. Although not visible at the scale of Fig. 4, additional small vortices appear in the corners of the rearward-facing steps at the rear shoulder and base of the probe. Finally, by $t = 1640.5$ s, a well-developed secondary vortex
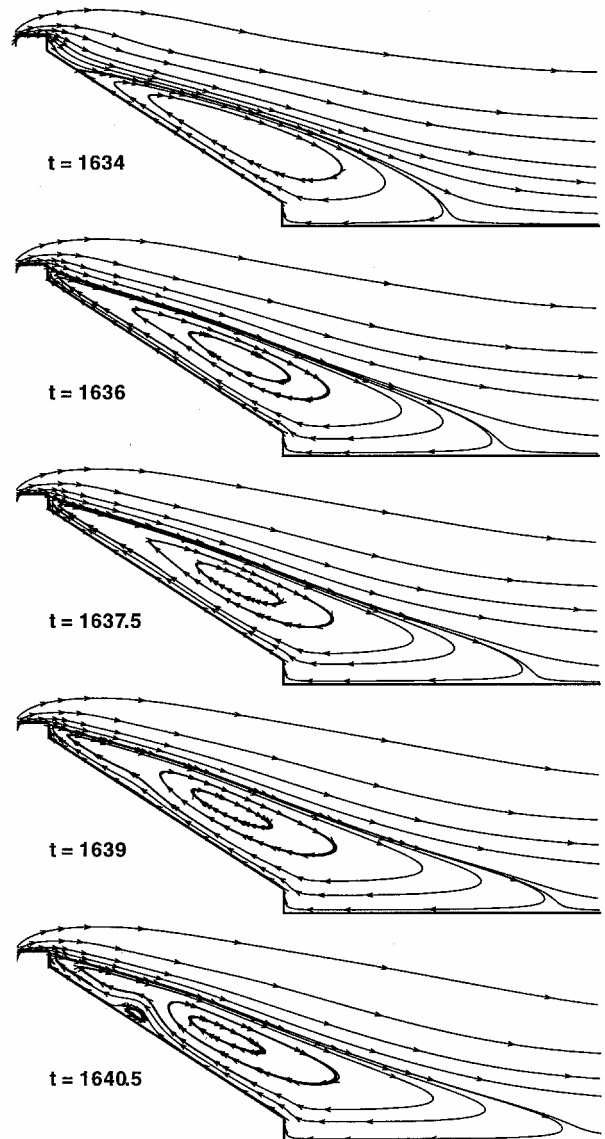

t = 1634

t = 1636

t = 1637.5

t = 1639

t = 1640.5

Fig. 4 Streamlines in the separated flow region for solutions between $t = 1634$ and 1640.5 s, showing evolution of the wake structure.

is apparent on the frustum. Although all computations predict these flows to be steady, it is likely that as the Reynolds number increases further the secondary vortices will begin to move, and the flow will become unsteady.[30]

Surface Heating

Figure 5a shows the computed total convective, $\dot{q}_{tot}$ and the catalytic component $\dot{q}_{cat}$ of the heat transfer to the surface at $t = 1639$ s. Data are plotted vs s, the pathlength distance from the apex of the vehicle. The surface was assumed to be noncatalytic to neutral species and fully catalytic to ions. The isothermal wall temperature, $T_w = 1325$ K, was taken from the forebody thermocouple data. The solution was obtained on the baseline 161×97 grid, with the wall spacing chosen to maintain a constant cell Reynolds number, $Re_c = 2$, on the surface. The effects of grid resolution and varying wall spacing will be examined. It is impossible to compare directly our forebody convective heating results to the experimental data, which are based on total (convective and radiative) heating. However, from Fig. 5a we see that the stagnation convective heating is about 330 W/cm^2, which is within 5% of the value reported by Olynick et al.[4] using a similar set of modeling assumptions. The catalytic component of heating is negligible on the entire surface, comprising about 2% of the total heat transfer. This is because most of the ions recombine in the cold boundary layer before reaching the surface.

The flow undergoes a pair of rapid expansions, first at the heatshield shoulder (point 1 in Fig. 5a) and then at the rearward facing step (point 2), which result in a local increase in heat transfer during the expansion, followed by a rapid decrease. An enlargement of the afterbody region is shown in Fig. 5b. The numbers in Fig. 5b correspond to the inset in Fig. 5a. Also included in Fig. 5b are the experimental data from each of the 12 calorimeters. Because the calorimeters were placed in a symmetrical array, there are three points at each s location, corresponding to different circumferential locations ϕ. The experimental data show that there is little circumferential data scatter, which is consistent with the small angle of attack, $\alpha < 1$ deg, reported during the first data period. However, the computation predicts a heat transfer rate that is considerably lower than the experimental data. Although not shown here, the same trend is observed for the other trajectory points. The rather poor comparison between the initial computations and the data is not too surprising, when the simplistic nature of the boundary conditions that were initially imposed at the surface is considered. In the next sections of the paper we look at several modeling assumptions that were made to determine their effect on computed heat transfer.

Grid Sensitivity

One possibility for the poor agreement between the computation and experiment is grid resolution. To examine this effect, grid refinement studies were conducted at the $t = 1634$ and 1639 s trajectory points, covering a range of Reynolds numbers between 2×10^4 and 1×10^5 based on body diameter. The number of grid points in the axial and normal directions as well as the body normal spacing and grid topology were varied to determine their effect on computed heat transfer. Grids were constructed that varied either the axial or normal point density while the other was held constant, so that effects of axial and normal resolution could be distinguished. This facilitated the final selection of a point density that ensured grid resolution.

Figure 6 shows representative results at $t = 1639$ s. Solutions are shown on five grids. Only the afterbody region is shown in Fig. 6; the forebody heat transfer varied by less than 1% on all grids tested. (Slightly larger deviations were seen at the stagnation point due to numerical issues with some of the grids.) The baseline grid, A, has 161 points along the body surface and 97 points in the normal direction. Wall spacing was chosen to maintain a constant cell Reynolds number, $Re_c = 2$, which implies that the near-wall spacing in the low-density afterbody is much larger than on the forebody. This resulted in a wall spacing on the afterbody of about 1×10^{-4} m at $t = 1639$ s. The second grid, B, was refined in the axial direction only, with 253 axial points clustered near the shoulder and geometric corners on the afterbody. The normal spacing was identical to the preceding grid. From Fig. 6, we see that the increased axial resolution lowered the predicted heat transfer by about 10%. This trend is consistent with the results of Olynick et al.,[34] who showed that the corner expansion plays a significant role in determining heat transfer on the afterbody for the Stardust sample return capsule. Based
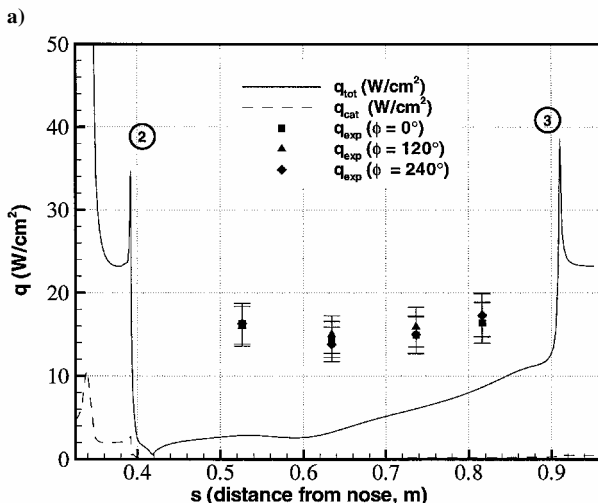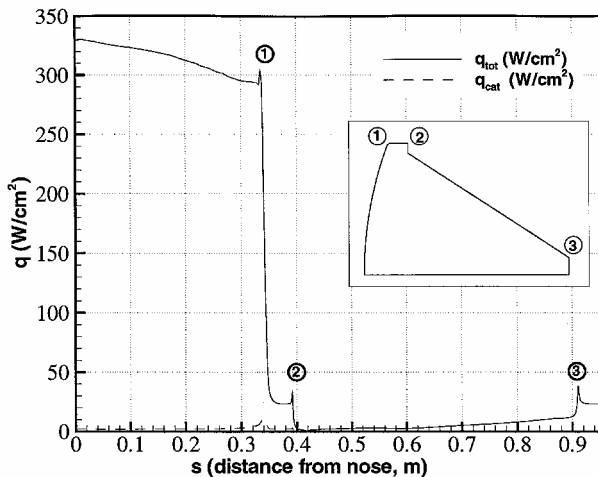

a)

b)

Fig. 5   Computed total convective, $\dot{q}_{tot}$, and catalytic component $\dot{q}_{cat}$ of heat transfer to the body surface at $t = 1639$ s: a) entire vehicle and b) enlargement of the afterbody region with experimental data from the 12 calorimeters.
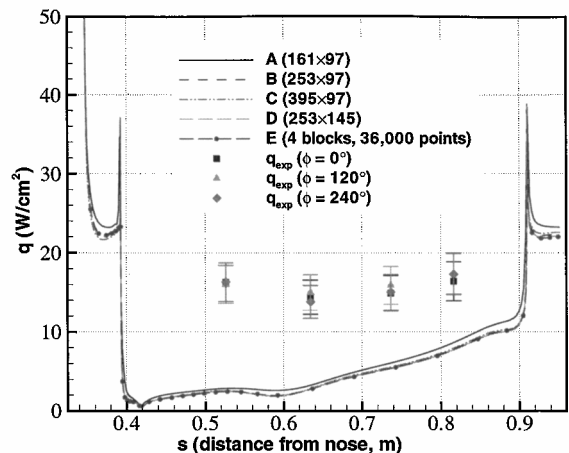

Fig. 6   Impact of grid resolution on the computed heat transfer at $t = 1639$ s.

on this result, a third grid, C, was generated, which had 395 points in the axial direction and the same normal distribution as the preceding grids. The solution on this grid was essentially the same as that obtained on grid B, indicating that grid B has sufficient axial resolution. Next, the normal resolution was increased. The fourth grid, D, was constructed with 253 axial points (same distribution as grid B) and 145 normal points. In addition, the wall spacing was reduced by a factor of two. There is essentially no difference between the solutions on grids B and D, indicating that the normal resolution of grid B is sufficient to resolve this flow.

The final solution shown in Fig. 6 was obtained on a four-block grid, E, with 36,000 total grid points (50% more than grid B). Axial spacing was identical to grid B (253 points on the surface); however the normal spacing was set to a constant value of 10^{-5} m over the entire surface, resulting in a cell Reynolds number of about 0.2 in the afterbody region. In addition, most of the extra points were clustered in the separated flow region using the compact enrichment technique described earlier. This resulted in approximately 150 points in the body-normal direction in the wake region, clustered such that most of the points were in the wake core. The computed heat transfer on this grid is essentially identical to that obtained on grid B, again indicating that at these low Reynolds numbers the near-wall spacing and normal resolution of the shear layer and separated flow region are not critical to predicting heat transfer. No unsteadiness was observed in any of the solutions obtained for this study.

A similar study was performed at $t = 1634$ s. At this point, the Reynolds number is a factor of five lower than at $t = 1639$ s, and as expected, there is less sensitivity to grid refinement. For this case, the computed afterbody heat transfer varied less than 5% on all grids tested. These results indicate that grid resolution is not the cause of the disagreement between the flight data and the computations.

Sensitivity to the Gas Thermal State

The effect of the assumed thermal state of the gas is shown in Fig. 7 for $t = 1639$ s. The thermal nonequilibrium solution is obtained using the method described earlier, and the equilibrium solution is computed using statistical mechanics to model the vibrational energy of the gas at the single temperature T. As seen in Fig. 7, the assumption of thermal equilibrium vs nonequilibrium has no impact on the computed heat transfer. The same is true for all other trajectory points as well. This result is because the postshock flow consists entirely of atomic species and their ions; there are essentially no molecules to carry the vibrational energy. Because the forebody wall boundary condition is noncatalytic to neutral species, there is little recombination occurring in the near-wall region on the forebody, and thus, the wake core will consist mainly of atoms as well. For example, at $t = 1639$ s the maximum mass fraction of diatomic species in the wake is less than 3%. However, for a less energetic flow, or for a forebody surface that is catalytic to neutrals, one would expect the thermal state of the gas to have a larger influence on the wake core.[34]
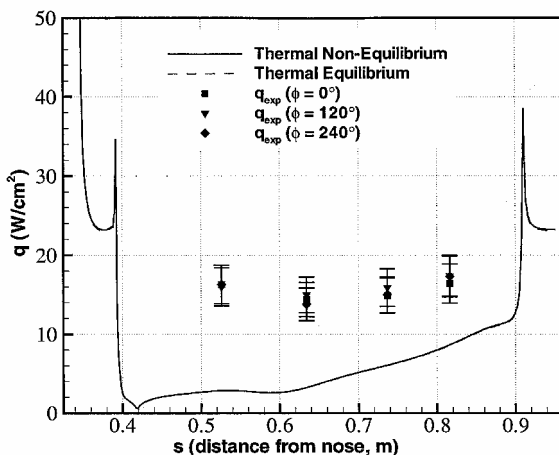

Fig. 7 Effect of the thermal state of the gas on computed afterbody heat transfer at $t = 1639$ s.
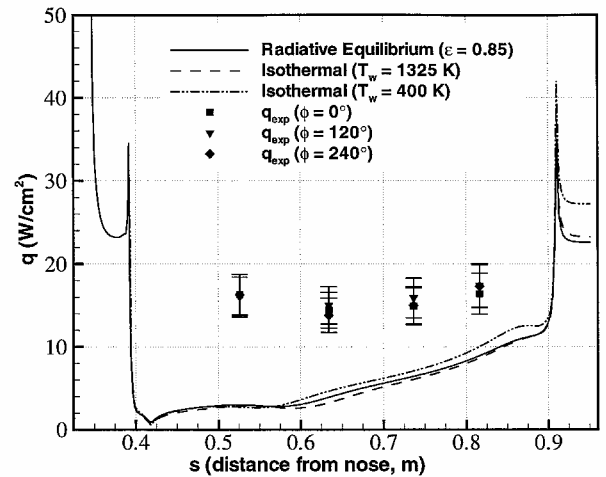

Fig. 8 Effect of the thermal wall boundary condition on computed afterbody heat transfer at $t = 1639$ s.

Sensitivity to Surface Temperature

In the preliminary computations an isothermal wall was assumed, with the wall temperature taken to be the same as that for the forebody. However, the materials used on the afterbody heat shield are much less conductive than the beryllium forebody. This would imply that perhaps a radiative equilibrium boundary condition would be more appropriate, in which conduction into the surface is assumed to be zero and the heat convected to the surface is balanced by that radiated away. Heat transfer to the surface then becomes a function of the surface temperature, given by $\dot{q}_{tot} = \epsilon \sigma T_w^4$. At the other extreme, we can use the thermocouple data directly to predict an afterbody temperature. The thermocouple data indicate a temperature of about 400 K at $t = 1639$ s. This temperature is slightly misleading because the thermocouples are attached to highly conductive gold calorimeter slugs, rather than the much less conductive phenolic–asbestos afterbody material. However, it provides another data point that can be used to assess the sensitivity of the heat transfer to the applied thermal boundary condition. Figure 8 shows the results of this analysis for $t = 1639$ s. Results are shown for a radiative equilibrium wall, $\epsilon = 0.85$, a "hot" isothermal wall, $T_w = 1325$ K, and a cold wall, $T_w = 400$ K. In each case the forebody temperature was held constant. The wall temperature on the conical frustum for the radiative equilibrium solution ranged from about 700 K at the beginning, $s = 0.42$ m, to about 1300 K at the end, $s = 0.90$ m. From Fig. 8 we see that decreasing wall temperature tends to increase surface heat transfer, although the increase on the frustum is small ($<10\%$) as compared the the discrepancy between the flight data and the computation. Interestingly, the flat base, $s > 0.91$ m, was more sensitive to the wall temperature, with the heat transfer increasing by more than 20% as the wall temperature was lowered from its radiative equilibrium value, 1500 K, to 400 K. However, because this region of the vehicle was simplified during construction of the OML, this effect was not explored further.

Sensitivity to Noncontinuum Effects

The solutions shown in this paper were obtained assuming a continuum flow. However, at these Reynolds numbers, noncontinuum effects may be present in the base region. To assess the importance of noncontinuum effects on computed heat transfer, the gradient length local Knudsen number, Kn_{GLL} (see Ref. 35) was computed for the $t = 1634$ and 1639 s trajectory points, with the results shown in Fig. 9. Following the work of Boyd et al.,[35] continuum break-down can be expected to begin when $Kn_{GLL} > 0.05$. From Fig. 9a we see that at $t = 1634$ s ($Re_D = 2 \times 10^4$) there are significant noncontinuum effects in the near-wall region of the afterbody. However, at $t = 1639$ s ($Re_D = 1 \times 10^5$) continuum breakdown is much less severe and is confined to the last third of the conical frustum and the flat base (Fig. 9b). Unfortunately, Boyd et al.[35] did not quantify the relationship between Kn_{GLL} and computed heat transfer. However, a Navier–Stokes solution in general will slightly overpredict heat
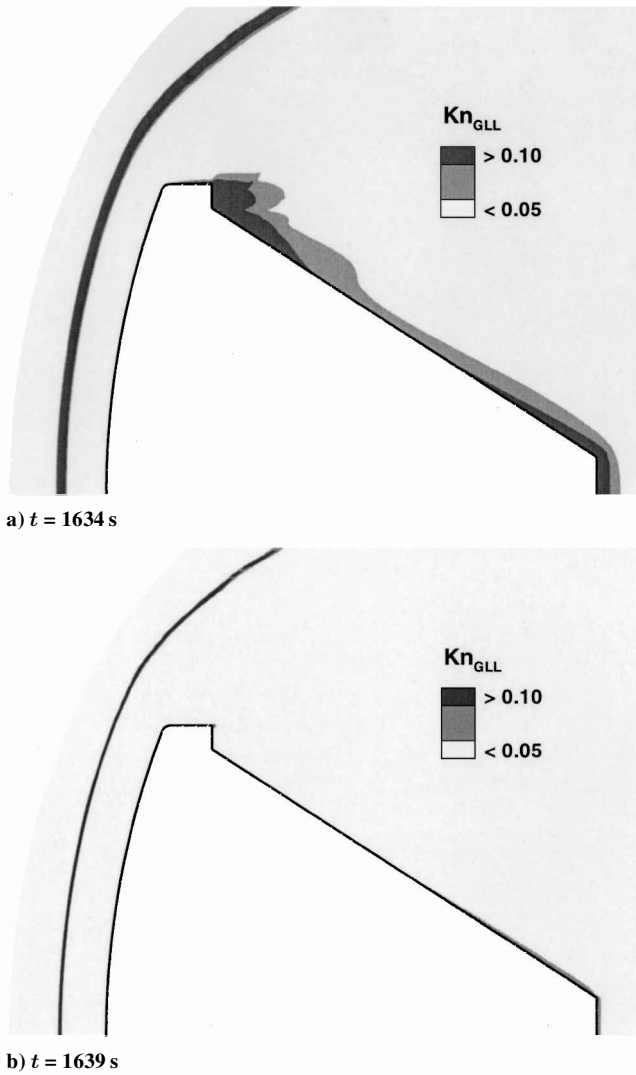
a) $t = 1634$ s

b) $t = 1639$ s

Fig. 9 Assessment of continuum flow assumption, as measured by the gradient length local Knudsen number, Kn_{GLL}.

a) $t = 1634$ s

b) $t = 1639$ s

Fig. 10 Comparison between heat transfer computed using several catalysis models on the afterbody with experimental data.

transfer in the base region of a noncontinuum flow (see Ref. 36). Slip wall boundary conditions would permit a more rigorous estimate of noncontinuum effects with a Navier–Stokes code and would capture this slight decrease in heat transfer. However, full implementation of a slip wall boundary condition in a reacting flow code is a nontrivial effort,[37] which has not been completed in DPLR-Axi at this time.

Sensitivity to Surface Catalysis

The afterbody surface was initially assumed to be noncatalytic to neutral species. However, because the wake core consists almost entirely of dissociated atoms, any surface catalycity would have a large impact on the heat transfer. Although the materials used in the construction of the Fire II afterbody heatshield are no longer in production, it is possible to draw some analogies to current materials. Based on analysis of silicon and carbon–phenolics, the surface coating and the underlying phenolic resin would likely start to pyrolyze when the surface temperature exceeded about 700 K. Vigorous pyrolysis would occur by about 800 K, and the process would be complete by the time the surface reached about 1100 K. The end product of this pyrolysis would be a surface layer of carbon char, which should be nearly fully catalytic. However, this char would be mixed with asbestos fibers, which are essentially a ceramic material with very low catalycity. As already stated, the surface temperature of the heat shield is not known accurately, which makes it difficult to predict the onset of pyrolysis. However, the effects of surface catalycity can be bounded by assuming a fully catalytic surface,
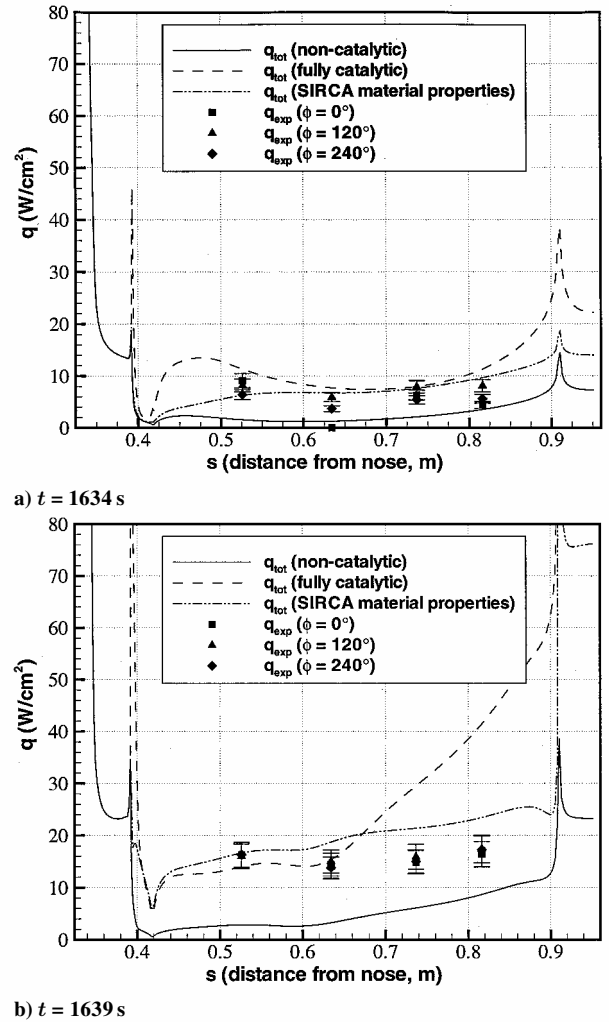
$\gamma_{neutrals} = \gamma_{ions} = 1$. In addition, a supposition is made that, before the onset of pyrolysis, the surface catalycity of the silicon-based coating would be similar to that of silicon-impregnated reusable ceramic ablators (SIRCA),[38] for which accommodation coefficients for nitrogen and oxygen recombination as a function of temperature are known.[39]

Based on this analysis, solutions are obtained for each of the five trajectory points on the baseline grid, assuming an afterbody surface that is noncatalytic, fully catalytic, and partially catalytic using the rates for SIRCA. In all cases, a radiative equilibrium wall is assumed. Results for $t = 1634$ s are shown, together with the experimental data, in Fig. 10a. The assumption of catalysis on the afterbody significantly increases predicted heat transfer. As expected,[40] both catalytic solutions show a pronounced catalytic "spike" at the rear of the shoulder, $s = 0.38$ m, where the highly dissociated gas flows over the surface transition from a noncatalytic to a catalytic surface. In addition, both solutions predict much higher heating on the flat base. This result is because the flow is separated, and thus, the highly dissociated wake flow first comes in contact with the catalytic surface in the base. As the reverse flow travels forward on the frustum, the flow rapidly recombines, depositing its energy preferentially on the trailing end of the frustum. This effect is less pronounced for the SIRCA case, both because less catalysis is occurring and because the SIRCA rates are temperature dependent. The hump in heat transfer for the fully catalytic solution around $s = 0.45$ m is due to that the flow does not separate at the corner at this low Reynolds number (Fig. 4), and thus, there is a region of dissociated forward flow on the first part of the frustum. Once again, there is little scatter in the experimental data, with the exception of a spurious zero reading at

$s = 0.63$ m and $\phi = 0$ deg. The noncatalytic solution significantly underpredicts the data, which is consistent with the results shown earlier for $t = 1639$ s. However, the fully catalytic solution slightly overpredicts the data, whereas the partially catalytic SIRCA solution is generally in good agreement.

Figure 10b shows the same results for $t = 1639$ s. For this case, the catalytic jumps at the rear of the shoulder and on the flat base are much larger, as expected. The SIRCA computation shows the best agreement with the data, although the heat transfer is overpredicted at the final two s locations. The fully catalytic afterbody solution drastically overpredicts heating at these locations. Interestingly, the fully catalytic solution predicts lower heat transfer on the forward part of the frustum for this case than the SIRCA solution. This effect appears to be because, for the fully catalytic case, much of the recombination (and associated heat release) is occurring at the back end of the frustum, whereas for SIRCA the slower recombination rates result in catalytic heat release along the entire surface.

The trends in the data become clearer if we plot heat transfer vs time at each calorimeter location, as shown in Fig. 11 for each of the four x/L calorimeter locations, where $x/L = 0$ at the rearward-facing step on the heatshield shoulder and $x/L = 1$ at the theoretical apex of the conic frustum. In Fig. 11, the solid lines are the experimental data from the three circumferentially distributed calorimeters at each x/L location, the dashed lines represent the assumed $\pm 15\%$ uncertainty in the experimental data, and the symbols are the results of the CFD computations for a noncatalytic, fully catalytic, and SIRCA surface. From Fig. 11, we see that the noncatalytic predictions are low throughout the trajectory. The fully catalytic and SIRCA predictions show good agreement with the data

at $x/L = 0.19$ and 0.38 over the entire trajectory range examined here. However, at $x/L = 0.58$ and 0.70, a different trend is seen. Whereas the SIRCA prediction is in good agreement with the data up to $t = 1637.5$ s, the fully catalytic solution has begun to overpredict heating significantly by this time. In addition, as t increases, the heat transfer predicted by both catalytic solutions continues to rise, although the flight data appear to level off at 15–17 W/cm^2. From a design standpoint, some comfort can be taken from the fully catalytic prediction being conservative over the later (highest heating) portion of the trajectory. However, the amount of conservatism in this solution on the last half of the frustum would lead to unnecessarily large margins on the heat shield thickness if it were used as a basis for design.

Figure 12 shows the experimental heating data for $x/L = 0.56$ over the entire trajectory. Profiles at the other locations have a similar shape. Also shown in Fig. 12 is the total (convective and radiative) heat transfer measured at the forebody stagnation point. Gaps in the forebody heating data correspond to periods of calorimeter melting and ejection. From Fig. 12, it is clear that the afterbody heating on the frustum reached a maximum about 6 s earlier than the forebody stagnation point. This result is contrary to computations used for Stardust heatshield design[34] and flight data from a thermocouple located on the conical frustum of the Mars Pathfinder entry vehicle,[41] which both showed that maximum heating on the afterbody frustum occurred concurrent with or after forebody peak heating. This discrepancy implies that there was some physical process occurring during the Fire II entry that was not observed in the Stardust computations or the Pathfinder entry. It is difficult to identify the mechanism that caused the experimental heat transfer to level off
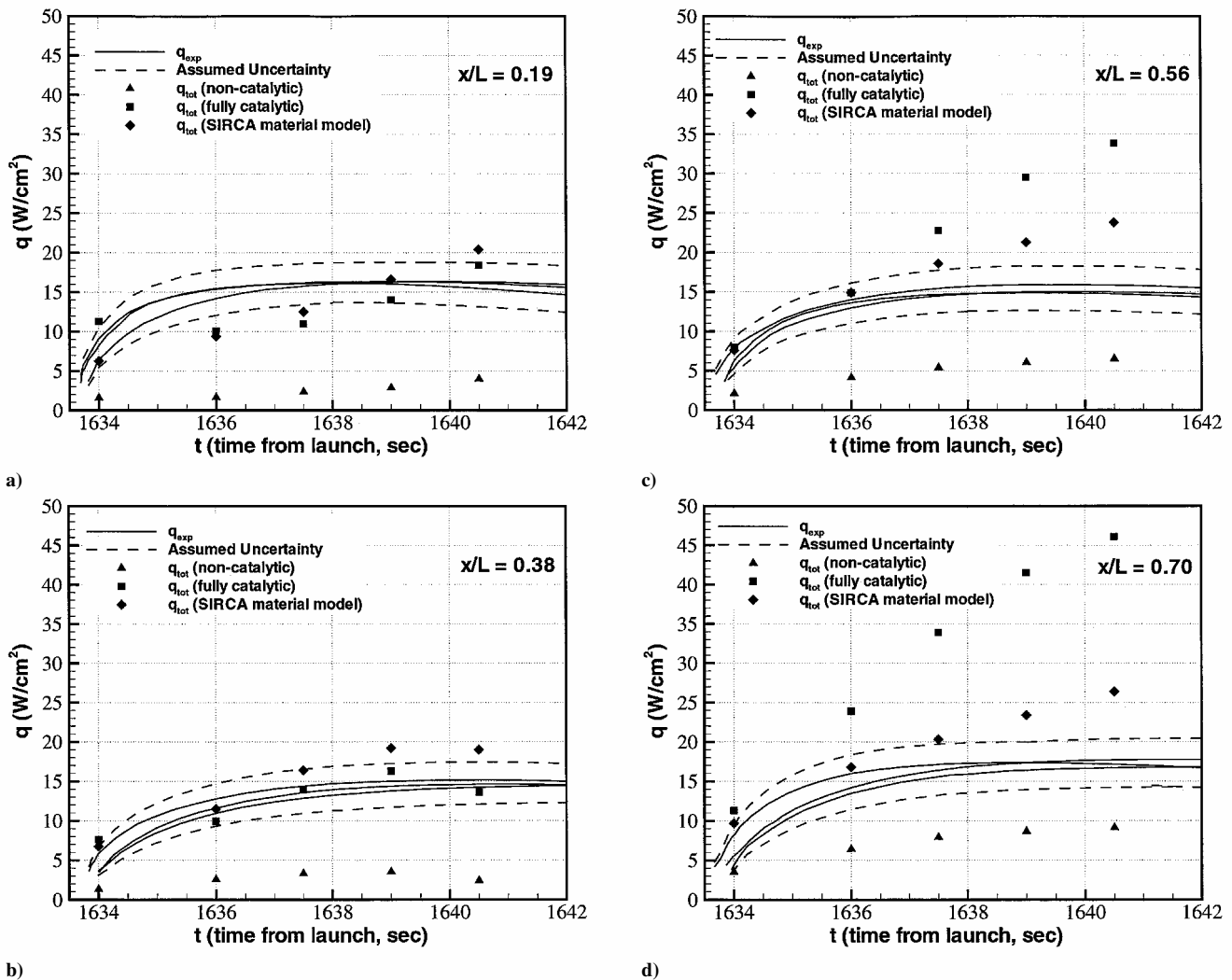

Fig. 11 Time histories of total heat transfer computed using several catalysis models on the afterbody as compared to flight data, x and L defined in Fig. 1: a) $x/L = 0.19$, b) $x/L = 0.38$, c) $x/L = 0.56$, and d) $x/L = 0.70$.
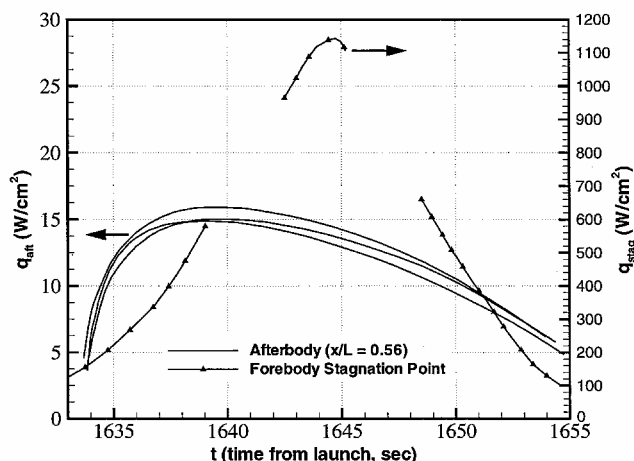
Fig. 12 Time histories of total heat transfer measured during flight on conical frustum at $x/L = 0.56$ and at forebody stagnation point; gaps in forebody heat transfer curve correspond to periods of heatshield melting and ejection.

at around $t = 1638$ s without a more detailed investigation of the material response of the surface. However, one possibility is that pyrolysis is beginning at around this time. The onset of pyrolytic blowing would reduce the heat transfer to the surface over that predicted here. Pyrolysis did not occur on the Pathfinder afterbody because peak heat transfer rates were an order of magnitude smaller than those encountered by Fire II. Another possibility is the assumption of a noncatalytic forebody. If the forebody were partially catalytic to neutrals, the concentration of atoms in the wake core would be reduced, lowering the magnitude of the catalytic jump at the trailing end of the frustum and on the base plate.

Conclusions

The wake flow and afterbody heating environment of the Project Fire II flight experiment were simulated using CFD. Results were obtained over the first portion of the trajectory, spanning the period from the onset of significant afterbody heating to the peak heating point. Computed heat transfer on the conical frustum portion of the afterbody was compared to the flight data. Although forebody heating results showed excellent agreement with previous computations, the initial noncatalytic predictions of afterbody heating were about a factor of two below the experimental values. Grid resolution of the solutions was confirmed, and some of the modeling assumptions used during the CFD simulations were examined as possible sources of error. This analysis pointed to the possibility that catalysis was occurring on the afterbody heat shield. Computations were then made assuming both a fully catalytic afterbody surface and a partially catalytic surface using a material model for SIRCA, which was chosen to approximate the catalytic properties of the surface coating before the onset of pyrolysis. The computations including finite rate catalysis, particularly the SIRCA model, are in good in good agreement with the data over the early portion of the trajectory. However, the catalytic results are conservative near the peak afterbody heating point, especially on the rear portion of the conical frustum. Comparison of the computations and flight data from Fire II with previous data suggests that another mechanism, possibly pyrolysis, may be occurring during this portion of the flight, reducing the total heat transfer over the predictions that do not include material response. Although more work needs to be done, these results give increased confidence in the ability of CFD to predict, both conservatively and accurately, the afterbody heating environment of a planetary entry vehicle during the laminar portion of the trajectory.

Acknowledgments

References

[1]Cornette, E. S., "Forebody Temperatures and Calorimeter Heating Rates Measured During Project Fire II Reentry at 11.35 km/s," NASA TM X-1305, Nov. 1966.

[2]Cauchon, D. L., "Radiative Heating Results from the Fire II Flight Experiment at Reentry Velocity of 11.4 km/s," NASA TM X-1402, July 1967.

[3]Slocumb, T. H., "Project Fire II Afterbody Temperatures and Pressures at 11.35 Kilometers Per Second," NASA TM X-1319, Dec. 1966.

[4]Olynick, D. R., Henline, W. D., Hartung-Chambers, L., and Candler, G. V., "Comparisons of Coupled Radiative Navier–Stokes Flow Solutions with the Project Fire II Flight Data," *Journal of Thermophysics and Heat Transfer*, Vol. 9, No. 4, 1995, pp. 586–594.

[5]Greendyke, R. B., and Hartung, L. C., "Convective and Radiative Heat Transfer Analysis for the Fire II Forebody," *Journal of Spacecraft and Rockets*, Vol. 31, No. 6, 1994, pp. 986–992.

[6]Gokcen, T., "Computation of Nonequilibrium Radiating Shock Layers," *Journal of Thermophysics and Heat Transfer*, Vol. 9, No. 1, 1995, pp. 34–40.

[7]Balakrishnan, A., Park, C., and Green, M. J., "Radiative Viscous Shock Layer Analysis of Fire, Apollo, and PAET Flight Data," *Thermophysical Aspects of Reentry Flows*, edited by J. N. Moss, Vol. 103, Progress in Astronautics and Aeronautics, AIAA, New York, 1986, pp. 514–540.

[8]Gupta, R. N., "Navier–Stokes and Viscous Shock-Layer Solutions for Radiating Hypersonic Flows," AIAA Paper 87-1576, June 1987.

[9]Zappa, O. L., and Reinecke, W. G., "An Experimental Investigation of Base Heating on Typical Mars Entry Body Shapes," NASA CR-1920, Nov. 1971.

[10]Slocumb, T. H., "Project Fire I Heating and Pressure Measurements on the Reentry-Vehicle Afterbody at a Velocity of 38,000 Feet Per Second," NASA TM X-1178, Nov. 1965.

[11]Lewis, J. H., and Scallion, W. I., "Flight Parameters and Vehicle Performance for Project Fire Flight II, Launched May 22, 1965," NASA TN D-3569, Aug. 1966.

[12]Lee, J. H., "Basic Governing Equations for the Flight Regimes of Aeroassisted Orbital Transfer Vehicles," *Thermal Design of Aeroassisted Orbital Transfer Vehicles*, edited by H. F. Nelson, Vol. 96, Progress in Astronautics and Aeronautics, AIAA, New York, 1985, pp. 3–53.

[13]Candler, G. V., "The Computation of Weakly Ionized Flows in Chemical Nonequilibrium," Ph.D. Thesis, Dept. of Aeronautics and Astronautics, Stanford Univ., Stanford, CA, 1988.

[14]Gnoffo, P. A., Gupta, R. N., and Shinn, J. L., "Conservation Equations and Physical Models for Hypersonic Air Flows in Thermal and Chemical Nonequilibrium," NASA TP 2867, Feb. 1989.

[15]Park, C., "Review of Chemical-Kinetic Problems of Future NASA Missions, Part 1: Earth Entries," *Journal of Thermophysics and Heat Transfer*, Vol. 7, No. 3, 1993, pp. 385–398.

[16]Wilson, J., "Ionization Rates of Air Behind High Speed Shock Waves," *Physics of Fluids*, Vol. 9, No. 10, 1966, pp. 1913–1921.

[17]Millikan, R. C., and White, D. R., "Systematics of Vibrational Relaxation," *Journal of Chemical Physics*, Vol. 39, No. 12, 1963, pp. 3209–3213.

[18]Gupta, R. N., Yos, J. M., Thompson, R. A., and Lee, K., "A Review of Reaction Rates and Thermodynamic and Transport Properties for an 11-Species Air Model for Chemical and Thermal Nonequilibrium Calculations to 30,000 K," NASA RP 1232, Aug. 1990.

[19]Bartlett, E. P., Kendall, R. M., and Rindal, R. A., "An Analysis of the Coupled Chemically Reacting Boundary Layer and Charring Ablator: Part IV—A Unified Approximation for Mixture Transport Properties for Multicomponent Boundary-Layer Applications," NASA CR 1063, June 1968.

[20]Lees, L., "Hypersonic Wakes and Trails," *AIAA Journal*, Vol. 2, No. 3, 1964, pp. 417–428.

[21]Park, C., *Nonequilibrium Hypersonic Aerothermodynamics*, Wiley, New York, 1990, p. 141.

[22]Pope, R. B., "Stagnation Point Convective Heat Transfer in Frozen Boundary Layers," *AIAA Journal*, Vol. 6, No. 4, 1968, pp. 619–626.

[23]Winkler, E. L., and Sheldahl, R. E., "Influence of Calorimeter Surface Treatment on Heat Transfer Measurements in Arc-Heated Test Streams," *AIAA Journal*, Vol. 4, No. 4, 1966, pp. 715, 716.

[24]Wright, M. J., Candler, G. V., and Bose, D., "A Data-Parallel Line Relaxation Method for the Navier–Stokes Equations," *AIAA Journal*, Vol. 36, No. 9, 1998, pp. 1603–1609.

[25]MacCormack, R. W., and Candler, G. V., "The Solution of the Navier–Stokes Equations Using Gauss–Seidel Line Relaxation," *Computers and Fluids*, Vol. 17, No. 1, 1989, pp. 135–150.

[26]Yee, H. C., "A Class of High-Resolution Explicit and Implicit Shock Capturing Methods," NASA TM 101088, Feb. 1989.

[27]Olejniczak, J., and Fletcher, D. G., "An Experimental and Computational Study of the Freestream Conditions in an Arc-Jet Facility," AIAA Paper 2000-2567, June 2000.

[28]Wright, M. J., Sinha, K., Olejniczak, J., Candler, G. V., Magruder, T. D., and Smits, A. J., "Numerical and Experimental Investigation of Double-Cone Shock Interactions," *AIAA Journal*, Vol. 38, No. 12, 2000, pp. 2268–2276.

[29]Gnoffo, P. A., Price, J. M., and Braun, R. D., "Computation of Near Wake Aerobrake Flowfields," *Journal of Spacecraft and Rockets*, Vol. 29, No. 2, 1992, pp. 182–189.

[30]Haas, B. L., and Venkatapathy, E., "Mars Pathfinder Computations Including Base-Heating Predictions," AIAA Paper 95-2086, June 1995.

[31]"Gridgen Users Manual," Ver. 12, Pointwise, Inc., Bedford, TX, 1997.

[32]Davies, C. B., and Venkatapathy, E., "The Self-Adaptive Grid Code SAGE, Version 3," NASA TM 208792, Aug. 1999.

[33]"GridPro/az3000 Users Guide and Reference Manual," Program Development Corp., White Plains, NY, 1996.

[34]Olynick, D. R., Chen, Y.-K., and Tauber, M. E., "Aerothermodynamics of the Stardust Sample Return Capsule," *Journal of Spacecraft and Rockets*, Vol. 36, No. 3, 1999, pp. 442–462.

[35]Boyd, I. D., Chen, G., and Candler, G. V., "Predicting Failure of the Continuum Fluid Equations in Transitional Hypersonic Flows," *Physics of Fluids*, Vol. 7, No. 1, 1995, pp. 210–219.

[36]Dogra, V. K., Moss, J. N., Wilmoth, R. G., Taylor, J. C., and Hassan, H. A., "Effects of Chemistry on Blunt Body Wake Structure," *AIAA Journal*, Vol. 33, No. 3, 1995, pp. 463–469.

[37]Gupta, R. N., Scott, C. D., and Moss, J. N., "Slip Boundary Conditions for Multicomponent Nonequilibrium Airflow," NASA TP 2452, Nov. 1985.

[38]Tran, H., Johnson, C., Rasky, D., and Hui, F., "Silicon Impregnated Reusable Ceramic Ablators for Mars Follow-on Missions," AIAA Paper 96-1819, June 1996.

[39]Stewart, D. A., "Surface Catalysis and Characterization of Proposed Candidate TPS for Access-to-Space Vehicles," NASA TM 112206, July 1997.

[40]Prabhu, D. K., Venkatapathy, E., Kontinos, D. A., and Papadopoulos, P., "X-33 Catalytic Heating," AIAA Paper 98-2844, June 1998.

[41]Milos, F. S., Chen, Y.-K., Congdon, W. M., and Thornton, J. M., "Mars Pathfinder Entry Temperature Data, Aerothermal Heating, and Heatshield Material Response," *Journal of Spacecraft and Rockets*, Vol. 36, No. 3, 1999, pp. 380–391.